Received: 15 May 2024 | Accepted: 3 September 2024

DOI: 10.1002/pamm.202400093

RESEARCH ARTICLE

An automatic simulation pipeline for coupled simulations of acoustic damping materials

Lars Radtke[1] | **Paul Marter**[2] | **Sascha Eisenträger**[2] | **Daniel Juhre**[2] | **Alexander Düster**[1]

[1]Numerical Structural Analysis with Application in Ship Technology (M-10), Hamburg University of Technology, Hamburg, Germany

[2]Institute of Mechanics, Otto von Guericke University Magdeburg, Magdeburg, Germany

Correspondence
Lars Radtke, Numerical Structural Analysis with Application in Ship Technology (M-10), Hamburg University of Technology, Am Schwarzenberg-Campus 4 C, 21073 Hamburg, Germany.
Email: lars.radtke@tuhh.de

Funding information
Deutsche Forschungsgemeinschaft, Grant/Award Numbers: DU 405/20-1, 503865803, EI 1188/3-1, 497531141

Abstract

Foamed materials are widely used to reduce noise due to their comparably good acoustic damping behavior. However, out of a large variety of these materials a suitable candidate has to be identified for each application. This is a challenging process that is typically guided by experiments and experience. While numerical simulations could support these experiments and reduce the effort to a great extent, no suitable discretization approach has yet been established that can fully capture the complex geometry of the foam. A fully resolved model is desirable in order to yield reliable predictions that can then be used to establish homogenized models. We established a monolithic coupling approach based on the finite cell method (FCM) that realizes a vibroacoustic simulation in this sense. The fluid and the structure domain are discretized by Cartesian grids and the geometry defined based on computed tomography scans is accounted for during the quadrature of the weak form. Our simulation in the time domain makes use of explicit time marching schemes and is therefore limited by a critical time step size. This is known to be arbitrarily low for discretizations with the FCM containing cells with arbitrarily small support. As a remedy against this we use the classical α-stabilization technique and investigate its potentials and limitations.

1 | INTRODUCTION

The selection of suitable acoustic damping materials for industrial applications is a typical challenge faced throughout the design process of various engineering systems and oftentimes lasts well into the prototyping stage or even until the installation of the product in its final working environment. This is due to the fact that the environment has a profound impact on the acoustic behavior of a system and leads to the need for a trial and error procedure on site to select suitable damping materials. Predictive numerical methods for such situations are generally available; however, they are currently not able to take into account the microstructure of foamed damping materials. Instead, homogenized material models are used, see, for example [1]. Using immersed boundary methods, the essentially impractical mesh generation process for complex geometries like those of foams can be circumvented. To this end, we develop a fully automatic simulation pipeline that takes as an input computed tomography (CT) scans of a foam specimen and yields as an output static and dynamic responses based on coupled simulations that account for the foam itself as well as the surrounding fluid (typically air).

Our simulations are based on the finite cell method (FCM) originally proposed in ref. [2]. It is a fictitious domain method combined with high-order shape functions, that is, the p-version of the finite element method (FEM). Aiming at transient simulations based on explicit time integration schemes, we do not rely on hierarchic basis functions as oftentimes done in this context (see, e.g., [3]) but on Lagrange shape functions. In particular, we use Lagrange polynomials based on Gauss-Lobatto-Legendre (GLL) points, which are used as a basis for the quadrature of the mass matrix as well leading to a diagonal mass matrix. In the boundary fitted context this yields the so-called spectral element method (SEM), which is not only favorable for transient problems because of the increased efficiency due to the diagonal mass matrix but also because of the increased accuracy by a factor of p (the polynomial degree of the shape functions). The SEM was mathematically investigated in ref. [4] and numerically in the context of structural mechanics in ref. [5]. In refs. [6, 7] the so called spectral cell method (SCM) was introduced as a combination of the SEM basis and quadrature with the FCM. In particular, different lumping schemes for cut cells that do not directly allow for an application of the GLL quadrature were investigated therein. Since then, the FCM was applied to transient problems in several applications, ranging from machine elements [8] to structural health monitoring [9].

More recently, lumping strategies for immersed boundary methods have gained a lot of interest. Ref. [10] provides a thorough investigation of immersed boundaries and mass lumping for Lagrange and B-spline basis function in the context of explicit dynamics. It also gives an overview of the most recent developments in this field. Another aspect investigated in refs. [11, 10] is the effect of immersed boundaries on the critical time step size. It is shown that Lagrange shape functions lead to increasing largest eigenvalues for decreasing supports of cut elements in the physical domain. For typical explicit time integration schemes like the central difference method (CDM) this leads to decreasing critical time step sizes and makes a direct application of the SCM impractical for problems, where the support of cut elements may become arbitrarily small. In ref. [12] an implicit-explicit (IMEX) time integration scheme is proposed to address this problem. Further, the eigenvalue stabilization technique developed for nonlinear static problems in ref. [13] was extended to transient problems in ref. [14] and can effectively increase the critical time step size. In this work, however, we only apply the classical α-stabilization as in refs. [6–8, 15].

The research is divided into two parts, where our focus lies on the identification of the static material parameters by means of advanced simulation techniques. On the other hand, experimental investigations are detailed in ref. [16], where compression tests are conducted to characterize the foam materials. The proposed simulation pipeline is used to perform the compression test numerically based on CT scans of the different foam specimens. The results are compared to the experiments in order identify the parameters for a material model that describes the bulk material the foam is made of. This is done by evaluating homogenized quantities, namely the load-displacement relationship, and tuning the material parameters in the fully resolved FCM model such that the results match the experiments. To this end, an isotropic material model is assumed and the anisotropic behavior is attributed to the foam geometry.

The remainder of this work is structured as follows. In Section 2 we briefly introduce the basic equations of vibroacoustics and their discretization. In Section 3 we give an overview of the simulation pipeline in order to show its potential in a general sense. In Section 4 we use the simulation approach to identify suitable parameters for the foam material based on experiments. While the identification is currently restricted to the static regime, we showcase the capabilities of the simulation approach in the dynamic regime based on a transient analysis in the time domain in Section 5. In Section 6 a conclusion and an outlook to future research directions is given.

2 | IMMERSED VIBROACOUSTICS

In this section, we recall the basic equations of vibroacoustics as well as their discretization using the FCM. For a more detailed formulation, we refer to ref. [17], where this simulation approach was introduced first.

2.1 | Governing equations

We consider a linear elastic structure within the domain Ω^{s} governed by the balance of linear momentum

$$\rho^{\mathrm{s}} \ddot{\boldsymbol{d}} - \operatorname{div}(\boldsymbol{\sigma}) = \boldsymbol{b}, \tag{1}$$

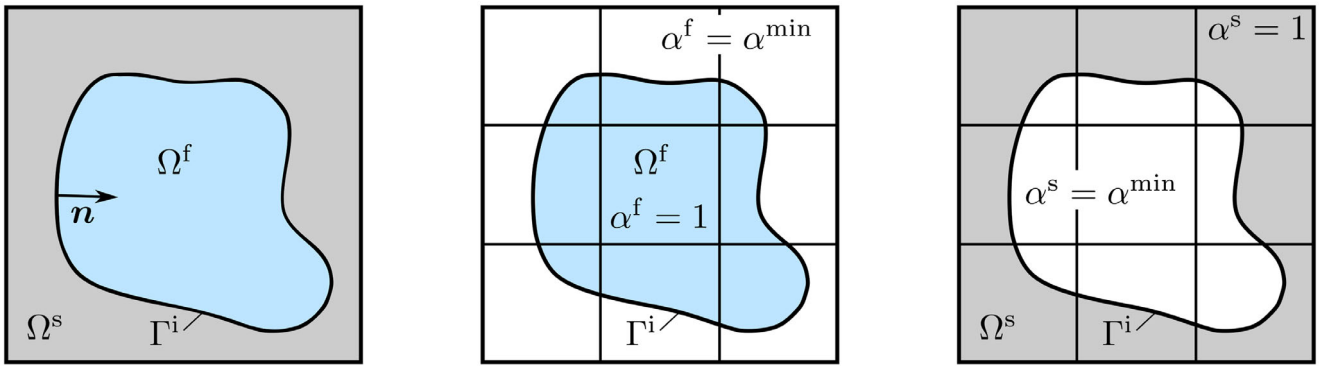

FIGURE 1 Discretization of the fluid domain Ω^{f} and the structure domain Ω^{s} using two independent FCM discretizations. FCM, finite cell method.

where ρ^{s} is the mass density, $\boldsymbol{d}$ is the displacement field, and $\boldsymbol{b}$ is a volumetric load. The Cauchy stress tensor $\boldsymbol{\sigma}$ is related to the engineering strain $\boldsymbol{\varepsilon}$ by

$$\boldsymbol{\sigma} = C\,\boldsymbol{\varepsilon}, \quad \text{with } \boldsymbol{\varepsilon} = \frac{1}{2}\left(\nabla \boldsymbol{d} + (\nabla \boldsymbol{d})^{\mathrm{T}}\right), \tag{2}$$

where C is the fourth-order elasticity tensor. For a more detailed introduction to computational structural dynamics we refer to refs. [18–20].

In another domain Ω^{f} we consider an acoustic fluid governed by the scalar wave equation

$$\ddot{\Psi} - \nabla \cdot \left(c^2\, \nabla \Psi\right) = f, \tag{3}$$

where $\Psi(\boldsymbol{x}, t)$ denotes the velocity potential, c is the wave velocity and f is a volumetric load. From Ψ, the acoustic pressure and the particle velocity can be recovered as

$$p^{\mathrm{f}} = \rho^{\mathrm{f}}\, \ddot{\Psi} \quad \text{and} \quad \boldsymbol{v}^{\mathrm{f}} = -\nabla \Psi, \tag{4}$$

where ρ^{f} denotes the fluid density.

The following coupling conditions are prescribed along the interface $\Gamma^{\mathrm{i}} = \Omega^{\mathrm{s}} \cap \Omega^{\mathrm{f}}$ to model the interaction between the two problems:

$$-\boldsymbol{\sigma}\,\boldsymbol{n} = p^{\mathrm{s}}\,\boldsymbol{n} = p^{\mathrm{f}}\,\boldsymbol{n} \quad \text{and} \quad \boldsymbol{v}^{\mathrm{f}} \cdot \boldsymbol{n} = \dot{\boldsymbol{d}} \cdot \boldsymbol{n}, \tag{5}$$

where $\boldsymbol{n}$ denotes the unit normal vector of Γ^{i} that points out of Ω^{s} and into Ω^{f}, see Figure 1 (left).

2.2 | Discretization

Figure 1 (middle and right) illustrates how the two problems are discretized using Cartesian grids that do not represent the actual geometry of the respective problem. Instead, indicator functions α^{f} and α^{s} are used to define the geometry, where

$$\alpha^{\mathrm{s}}(\boldsymbol{x}) = \begin{cases} 1 & \text{for } \boldsymbol{x} \in \Omega^{\mathrm{s}}, \\ \alpha^{\min} & \text{else} \end{cases} \quad \text{and} \quad \alpha^{\mathrm{f}}(\boldsymbol{x}) = \begin{cases} 1 & \text{for } \boldsymbol{x} \in \Omega^{\mathrm{f}}, \\ \alpha^{\min} & \text{else}\,. \end{cases} \tag{6}$$

If not stated otherwise, we set $\alpha^{\min} = 10^{-8}$. Further, we would like to note that choosing different values for $\alpha^{\min}$ on the fluid and the structure side is generally possible.

As in classical FEMs, a weak form is established that is then discretized. However, the weak form is based on the so-called extended domains $\Omega^{\mathrm{f}}_{\mathrm{e}}$ and $\Omega^{\mathrm{s}}_{\mathrm{e}}$ that are represented by the Cartesian grids. We introduce $\Gamma^{\mathrm{f,N}}$ and $\Gamma^{\mathrm{s,N}}$ as those parts of $\partial\Omega^{\mathrm{f}}$ and $\partial\Omega^{\mathrm{s}}$, where Neumann boundary conditions are prescribed but which are not part of Γ^{i}. Dirichlet boundary

conditions are prescribed in a strong sense later. After including the coupling conditions (5) and assuming that $\boldsymbol{\sigma}\,\boldsymbol{n} = \boldsymbol{t}$ on $\Gamma^{\mathrm{s,N}}$ as well as $\boldsymbol{v}^{\mathrm{f}} \cdot \boldsymbol{n} = \bar{v}$ on $\Gamma^{\mathrm{f,N}}$ we obtain

$$\int_{\Omega_{\mathrm{e}}^{\mathrm{s}}} \alpha^{\mathrm{s}}\, \rho^{\mathrm{s}}\, \ddot{\boldsymbol{d}} \cdot \delta\boldsymbol{d}\, \mathrm{d}\Omega_{\mathrm{e}}^{\mathrm{s}} + \int_{\Omega_{\mathrm{e}}^{\mathrm{s}}} \alpha^{\mathrm{s}}\, \boldsymbol{\varepsilon} \cdot \mathcal{C}\, \delta\boldsymbol{\varepsilon}\, \mathrm{d}\Omega_{\mathrm{e}}^{\mathrm{s}} + \int_{\Gamma^{\mathrm{i}}} \rho^{\mathrm{f}}\, \ddot{\Psi}\, \boldsymbol{n} \cdot \delta\boldsymbol{d}\, \mathrm{d}\Gamma^{\mathrm{i}} = \int_{\Omega_{\mathrm{e}}^{\mathrm{s}}} \alpha^{\mathrm{s}}\, \boldsymbol{b} \cdot \delta\boldsymbol{d}\, \mathrm{d}\Omega_{\mathrm{e}}^{\mathrm{s}} + \int_{\Gamma^{\mathrm{s,N}}} \boldsymbol{t} \cdot \delta\boldsymbol{d}\, \mathrm{d}\Gamma^{\mathrm{s,N}} \tag{7}$$

and

$$\int_{\Omega_{\mathrm{e}}^{\mathrm{f}}} \alpha^{\mathrm{f}}\, \ddot{\Psi} \cdot \delta\Psi\, \mathrm{d}\Omega_{\mathrm{e}}^{\mathrm{f}} + \int_{\Omega_{\mathrm{e}}^{\mathrm{f}}} \alpha^{\mathrm{f}}\, c^2\, \nabla\Psi \cdot \nabla\delta\Psi\, \mathrm{d}\Omega_{\mathrm{e}}^{\mathrm{f}} - \int_{\Gamma^{\mathrm{i}}} c^2\, \boldsymbol{n} \cdot \dot{\boldsymbol{d}}\, \delta\Psi\, \mathrm{d}\Gamma^{\mathrm{i}} = \int_{\Omega_{\mathrm{e}}^{\mathrm{f}}} \alpha^{\mathrm{f}}\, f\, \delta\Psi\, \mathrm{d}\Omega_{\mathrm{e}}^{\mathrm{f}} - \int_{\Gamma^{\mathrm{f,N}}} \bar{v}\, \delta\Psi\, \mathrm{d}\Gamma^{\mathrm{f,N}}. \tag{8}$$

Therein, $\delta\boldsymbol{\varepsilon}$ denotes the variation of $\boldsymbol{\varepsilon}$ and $\delta\Psi$ represents the variation of Ψ. For the illustrative problem shown in Figure 1 $\Omega_{\mathrm{e}}^{\mathrm{f}} = \Omega_{\mathrm{e}}^{\mathrm{s}} = \Omega^{\mathrm{s}} \cup \Omega^{\mathrm{f}}$. However, this is not necessarily the case.

Substituting the usual approximation based on finite element shape functions into Equations (7) and (8) we obtain the global system of equations

$$\begin{bmatrix} \mathbf{M}^{\mathrm{s}} & \mathbf{0} \\ \mathbf{0} & \mathbf{M}^{\mathrm{f}} \end{bmatrix} \begin{bmatrix} \ddot{\mathbf{U}}^{\mathrm{s}} \\ \ddot{\mathbf{U}}^{\mathrm{f}} \end{bmatrix} + \begin{bmatrix} \mathbf{0} & \mathbf{C}^{\mathrm{s}} \\ \mathbf{C}^{\mathrm{f}} & \mathbf{0} \end{bmatrix} \begin{bmatrix} \dot{\mathbf{U}}^{\mathrm{s}} \\ \dot{\mathbf{U}}^{\mathrm{f}} \end{bmatrix} + \begin{bmatrix} \mathbf{K}^{\mathrm{s}} & \mathbf{0} \\ \mathbf{0} & \mathbf{K}^{\mathrm{f}} \end{bmatrix} \begin{bmatrix} \mathbf{U}^{\mathrm{s}} \\ \mathbf{U}^{\mathrm{f}} \end{bmatrix} = \begin{bmatrix} \mathbf{f}^{\mathrm{s}} \\ \mathbf{f}^{\mathrm{f}} \end{bmatrix}. \tag{9}$$

Therein, $\mathbf{M}^{\mathrm{s}}$ and $\mathbf{M}^{\mathrm{f}}$ denote the mass matrices, $\mathbf{K}^{\mathrm{s}}$ and $\mathbf{K}^{\mathrm{f}}$ denote the stiffness matrices and $\mathbf{f}^{\mathrm{s}}$ and $\mathbf{f}^{\mathrm{f}}$ are the load vectors. For the coupling matrices we obtain $\mathbf{C}^{\mathrm{s}} = \rho^{\mathrm{f}}\, \mathbf{C}$ and $\mathbf{C}^{\mathrm{f}} = -c^2\, \mathbf{C}^{\mathrm{T}}$, where

$$\mathbf{C} = \int_{\Gamma^{\mathrm{i}}} \mathbf{N}^{\mathrm{s}\,\mathrm{T}}\, \boldsymbol{n}\, \mathbf{N}^{\mathrm{f}}\, \mathrm{d}\Gamma^{\mathrm{i}}. \tag{10}$$

The symbols $\mathbf{N}^{\mathrm{s}}$ and $\mathbf{N}^{\mathrm{f}}$ denote the interpolation matrices containing the shape functions in the usual way. For a more detailed explanation, see ref. [17].

2.2.1 | Shape functions

We use high-order Lagrange shape functions based on GLL points and combine them with a quadrature based on GLL points in elements that are not cut by the boundaries. This yields the so-called SEM, which is known for its high accuracy for dynamic problems of the present type and its efficiency when combined with explicit time integration schemes like the CDM. The increased accuracy compared to classical finite elements is related to a moderate underintegration of the mass matrix and can be achieved with any set of shape functions that spans the same space. The underintegration yields a discretization that approximates eigenvalues p times more accurate than the classical FEM, where p is the polynomial degree of the shape functions. This was mathematically proven in ref. [4] and investigated for structual mechanics in ref. [5]. Further, the eigenvalues in the SEM are underestimated (not overestimated as in the classical FEM), which is beneficial with regard to the critical time step size of explicit time integration schemes.

However, a combination of the spatial discretization based on GLL Lagrange shape functions and a GLL quadrature with explicit time integration schemes is especially efficient due to the mass matrix, which is diagonal by definition. Unfortunately, this is only the case for elements that are not cut by the boundary. Cut elements need a special quadrature rule due to the discontinuity of the integrands that is introduced by the indicator function α as will become clear in the next section. One possibility to restore the diagonality of the mass matrix is to apply classical lumping schemes. This was done in refs. [6, 21], where also tailored lumping schemes were developed and investigated. However, it is not clear in how far this affects the accuracy and convergence order of the resulting numerical method. In this work, we therefore do not apply any lumping to cut elements. In ref. [10] we have investigated the effect of lumping cut elements for Lagrange and B-Spline shape functions for one-dimensional problems and refer to it for further details.

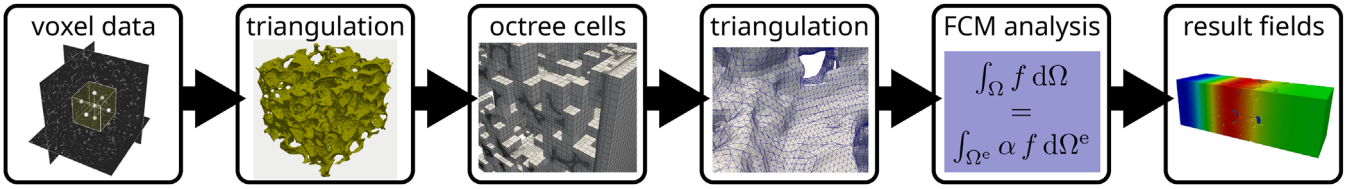

FIGURE 2 Major steps in the simulation pipeline.

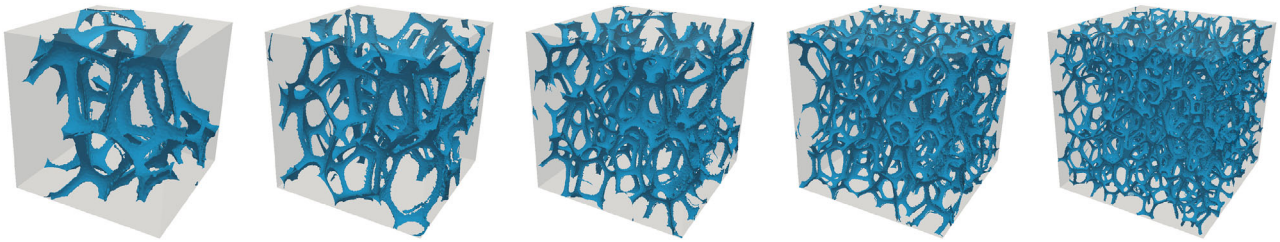

FIGURE 3 Cut-outs of different sizes from the foam geometry (left to right: 1, 1.5, 2, 2.5, and 3.4 mm).

2.2.2 | Quadrature

The integrals arising in the weak forms (7) and (8) can no longer be accurately integrated using standard quadrature rules. Instead, the discontinuities introduced by the indicator functions α^s and α^f have to be resolved. We use here the well established approach based on an octree. It is noted that alternative approaches that achieve the same accuracy with fewer quadrature points have been developed. They include smart space trees [22, 23], merging of sub-cells [24, 25] and boolean operations [26, 27]. Alternative quadrature rules such as moment fitting (see refs. [28–30]) are interesting in particular because they may allow to construct quadrature rules that yield a diagonal mass matrix even for cut cells as demonstrated in ref. [31]. However, these approaches cannot recover the accuracy of the SEM because the underintegration becomes too severe. Further, quadrature points outside of the physical domain are needed, which is problematic for nonlinear analyses.

2.3 | Time integration

We use the classical CDM to discretize Equation (9) in time. For a detailed formulation of the method, we refer to refs. [5, 17]. Important in the context of immersed boundary method is the critical time step size

$$\Delta t^{\mathrm{crit}} = \frac{2}{\omega_{\max}}. \tag{11}$$

Therein, $\omega_{\max}$ is the largest eigenfrequency of the system, that is, $\omega_{\max} = \sqrt{\lambda_{\max}}$, where $\lambda_{\max}$ is the largest eigenvalue of the generalized eigenvalue problem $(\mathbf{K} - \lambda\,\mathbf{M})\hat{\mathbf{U}} = \mathbf{0}$. We denote here with $\mathbf{K}$ and $\mathbf{M}$ the combined stiffness and mass matrix from Equation (9). As investigated in refs. [10, 11] Δt^{crit} becomes indefeasibly small, if elements with a very small support are present in the discretization. This situation cannot be avoided in the automatic simulation pipeline based on CT scans of foams such that stabilization techniques become inevitable.

3 | MODELING AND SIMULATION PIPELINE

The major steps in our fully automatic modeling and simulation pipeline are illustrated in Figure 2. The initial input is a CT scan of a foam specimen. In the first step, it is pre-processed and segmented to arrive at an analysis suitable triangulation of the foam surface. Figure 3 shows several cutouts from such a triangulation. The segmentation is a complicated procedure

in itself and further details are described in ref. [16]. Here we focus on the subsequent steps in the pipeline that directly relate to the FCM as described in the following.

3.1 | Construction of volume quadrature cells

In this step, the octree data structure is established. To this end, an inside-outside test is established and every element, respectively every cell, is subdivided into subcells if it is cut by the boundary. This is repeated for subcells up to a final tree depth of k. Any element that lies complete outside the physical domain is excluded from the analysis.

3.2 | Construction of interface quadrature cells

In order to compute the integrals over the coupling interface Γ^{i}, we have to provide quadrature cells for it as well. While a triangulation of the interface is already established within the segmentation process, we construct a second triangulation using the marching cubes algorithm in this step for two reasons:

1. It gives us full control over the resolution, that is, the number of triangles. This makes it possible to adapt the interface quadrature cells to the spatial discretization without the need to repeat the segmentation of the CT data.
2. It yields quadrature cells that resolve the finite element boundaries. This is important in order to accurately capture the discontinuities across element boundaries naturally arising for the chosen basis.

3.3 | Integration and stabilization of the system matrices

The last step towards the final FCM analysis is the integration and stabilization of the system matrices. To this end, the GLL quadrature is used for all uncut cells, while on cut cells, the standard Gauss-Legendre (GL) quadrature is used. Quadrature points outside of the physical domain are not excluded from the analysis, which in combination with a non-zero $\alpha^{\min}$ provides the only stabilization mechanism considered in this work. On the interface quadrature cells, the GL quadrature is used as well. Having established the quadrature cells and the distribution of quadrature points for all integration domains the subsequent evaluation of the integrands and assembly of the system matrices is done in the usual way.

3.4 | Time stepping and post-processing

The last step is to combine the system matrices for the fluid and the structure subproblem and perform the integration in time using the CDM. Like the previous steps in the pipeline, the postprocessing included in this step happens fully automatic. This includes means to evaluate quantities of interest at given locations or based on the mesh, the octree cells and the two available surface triangulations for visualization purposes.

4 | STATIC MATERIAL PARAMETER IDENTIFICATION

In this section, we present simulations from which the unknown parameters of the bulk material model can be identified based on given parameters of the homogenized model that were obtained from measurements. To begin with, we determine a suitable discretization by conducting h-convergence studies for several polynomial degrees p and partitioning depths k. Afterwards, convergence studies with regard to the considered domain size are conducted to determine a suitable representative volume element (RVE). Finally, the obtained information is used to identify the bulk material parameters assuming an isotropic behavior on the microscale.

Throughout this section, we consider static linear elastic problems only. Cube-shaped volumes with different edge length l_{d} are cut out from the triangulated foam geometry as shown in Figure 3. Figure 4 illustrates the simulation model including the octree cells for an exemplary domain size of $l_{\mathrm{d}} = 1.6\,\mathrm{mm}$. On one boundary in the y-z-plane a homogeneous Dirichlet boundary condition is applied. On the opposite side an almost rigid plate is attached. To this end, the computa-

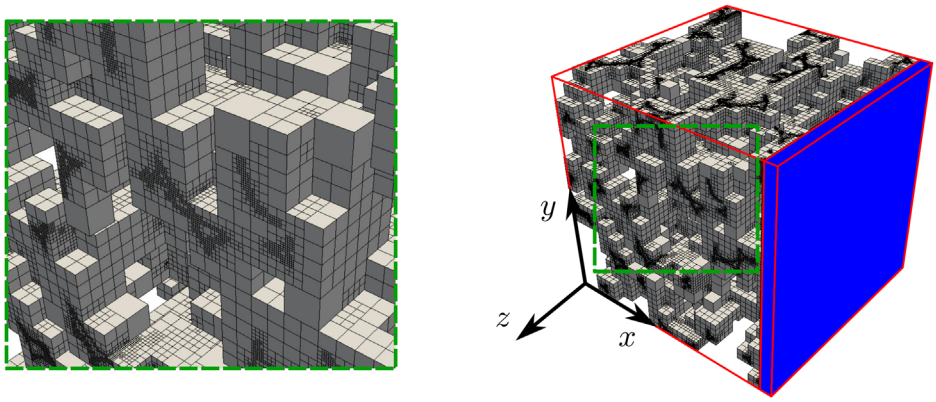

FIGURE 4 Illustration of the problem considered for the static material parameter identification.

tional domain is extended by l_b in the x-direction. On the corresponding outer boundary a Neumann boundary condition with a traction of $\boldsymbol{t} = [t_x\ 0\ 0]^\mathrm{T}$ is applied. At all remaining boundaries symmetry boundary conditions are applied. In order to avoid material interfaces within elements due to the almost rigid plate we choose

$$l_\mathrm{b} = \frac{l_\mathrm{d}}{n^\mathrm{e}},$$

where n^e is the number of elements used in each direction within the foam domain. The discretization of the overall computational domain with size $l_\mathrm{d} + l_\mathrm{b} \times l_\mathrm{d} \times l_\mathrm{d}$ is carried out using $n^\mathrm{e} + 1 \times n^\mathrm{e} \times n^\mathrm{e}$ elements. From the different simulations, the homogenized engineering strain in the x-direction is computed as

$$\bar{\varepsilon}_{xx} \approx \frac{d_x(\boldsymbol{x}_\mathrm{A})}{l_d}, \quad \text{with } \boldsymbol{x}_\mathrm{A} = [l_\mathrm{d}\ y\ z]\,,\ \boldsymbol{x}_\mathrm{A} \in \Omega. \tag{12}$$

For all computations of the strain in this way, we ensured that the result is independent of y and z.

4.1 | Convergence study

Due to the very fine discretizations, which are necessary to accurately capture the foam's elastic behavior, we do not compare our results to an overkill solution. Instead, we observe the quantity of interest, namely the homogenized strain $\bar{\varepsilon}_{xx}$, as the mesh is refined.

Figure 5 shows the results of the convergence study. As expected, it is observed that larger polynomial orders yield a higher accuracy per degree of freedom. However, we avoid even larger orders in view of the transient simulation, whose critical time step size is expected to decrease as p increases. Further, the larger the element size, the fewer elements are located completely outside of the physical domain and can be excluded from the simulation. The results further show that not only many degrees of freedom but also a sufficient partitioning depth of the octree cells is needed for a high accuracy. For further studies in this work, we select $p = 3$, $k = 5$ and an element size of $h = 0.05\,\mathrm{mm}$. This promises an acceptable accuracy in view of the discretization with $n^\mathrm{e} = 20$ for the domain size of $l_\mathrm{d} = 0.8\,\mathrm{mm}$ considered in the convergence study from Figure 5, where $h = 0.04\,\mathrm{mm}$.

4.2 | RVE

While a domain size of $l_\mathrm{d} = 0.8\,\mathrm{mm}$ was assumed to be sufficient for the convergence study, the smallest possible domain size that yields a RVE is still unknown. To this end, we perform simulations of the compression test as before but with constant element size of $h = 0.05\,\mathrm{mm}$ and increasing domain size. As the domain size l_d is increased, the number of elements n^e is adjusted accordingly to maintain the given element size.

Figure 6 shows the results obtained for different domain sizes. It is observed that from a domain size of $l_\mathrm{d} = 2.5\,\mathrm{mm}$ on the homogenized strain observed in the simulation stays constant. Accordingly, we use this domain size for the follow-

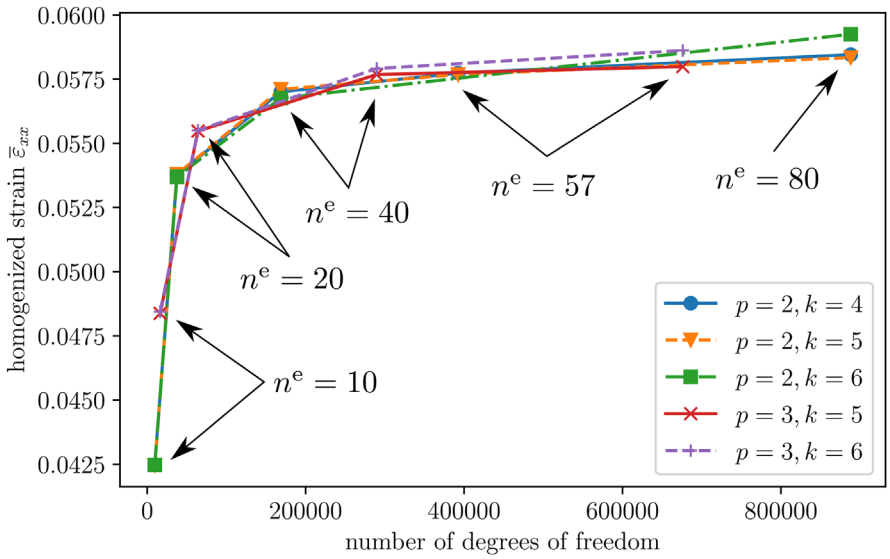

FIGURE 5 Convergence of the strain $\bar{\varepsilon}_{xx}$ in the problem from Figure 4 with a domain size of $l_d = 0.8$ mm under h-refinement.

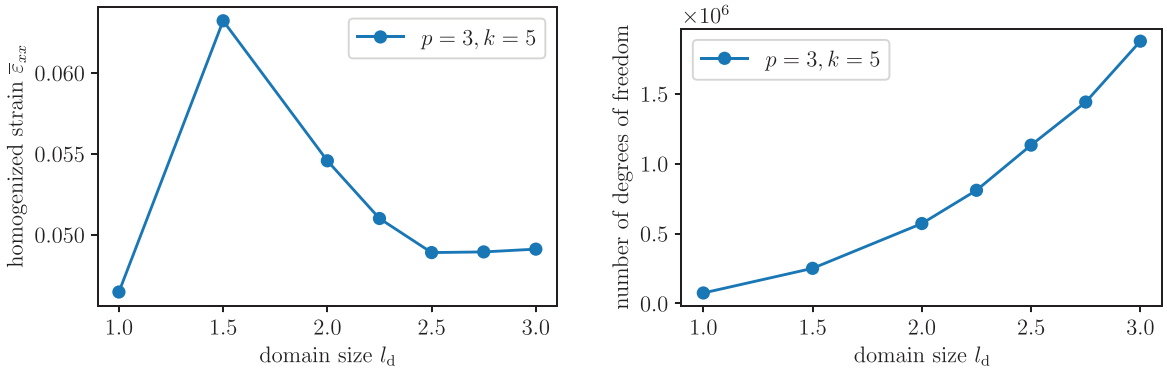

FIGURE 6 Convergence of the strain in the problem from Figure 4 as the domain size is increased.

ing investigations. Figure 6 (right) shows that we can expect around $1.25 \cdot 10^6$ degrees of freedom to be needed for this domain size.

4.3 | Bulk material parameters

In this section, we determine the bulk material parameters of the underlying polyurethane (PU). A measurement of these parameters is theoretically possible, for example, using uniaxial tensile tests of bulk specimens. However, we circumvent such tests for two reasons. First, we do not have suitable specimens of bulk material available. Second, we assume that the PU that makes up the struts in the foam is not actually homogeneous. Instead, it may contain very small inclusions of gas and show varying elastic properties due to the manufacturing process. Shortly spoken, we assume two different separations of scales: On the macro- (foam-) scale we assume that the foam shows a homogeneous behavior despite the foams micro-structure (pores and struts). On the meso- (strut-) scale, we assume that the individual struts behave homogeneously despite the micro-structure (small inclusions, etc.) of the bulk material whose parameters are to be identified. We further assume that this bulk material is isotropic (on the strut-scale) while we allow for orthotropic behavior in the homogenized model (on the foam-scale). Any orthotropic behavior observed here is thus attributed to the foams geometry.

4.3.1 | Simulation and experiment

As before, the homogenized strain $\bar{\varepsilon}_{xx}$ is evaluated from simulations of a foam specimen. Using the applied traction t_x and assuming that the homogenized Poisson ratio is zero the homogenized Young's modulus can be computed as

$$\bar{E}^{\mathrm{s}} = \frac{t_x}{\bar{\varepsilon}_{xx}} \tag{13}$$

and compared to experimental results, where it is evaluated in a corresponding way from force and displacement measurements. Thanks to the linearity of the elasticity problem, we can directly compute the Young's modulus of the bulk material as

$$E_i = \frac{\bar{E}_i^{\mathrm{m}}}{\bar{E}_i^{\mathrm{s}}} \tilde{E}. \tag{14}$$

Therein, $\tilde{E}$ denotes the assumed Young's modulus of the bulk material in the simulation and $\bar{E}_i^{\mathrm{m}}$ and $\bar{E}_i^{\mathrm{s}}$ denote the measured and simulated Young's modulus of the homogenized foam material, respectively. The index i refers to a rotation that is applied to the foam specimen prior to the simulation, respectively the experiment, in order to detect anisotropic behavior. Effectively, we perform the compression test along each of the three coordinate axes. For $i = 1$, the compression is applied in the thickness direction of the original foam sample which is provided as 30 mm thick plates from the manufacturer. The experiments are accordingly done using cube-shaped specimens with an edge-length of 30 mm. For a detailed description of the experiments, we refer to ref. [16]. The rotation $i = 2$ and $i = 3$ yield compression tests in the in-plane directions of the larger foam sample. It is noted here that the foam sample in the experimental compression tests is not the same as the one from the CT scan considered in the simulation.

4.3.2 | Fitting approaches

In order to illustrate the two purposes of the computations in this section, two different fitting strategies are applied. First, we only consider the rotation $i = 1$ and compute E_1 according to Equation (14). We then carry out simulations for the other coordinate directions using $\tilde{E} = E_1$ and compute $\bar{E}_2^{\mathrm{s}}$ and $\bar{E}_3^{\mathrm{s}}$ (knowing that $\bar{E}_1^{\mathrm{s}} = \bar{E}_1^{\mathrm{m}}$ by design of the fit). This serves the purpose of verifying our modeling assumptions as well as the solution method. Second, we use the simulations and experiments for $i = 2$ and $i = 3$ for the identification as well and compute also E_2 and E_3 according to Equation (14). We then determine the $\bar{E}_i^{\mathrm{s}}$ that results from choosing $\tilde{E} = \frac{1}{3}(E_1 + E_2 + E_3)$ to fit the results in a mean sense. This serves the purpose of finding the best possible value for the Young's modulus of the bulk material, that is, the one that yields the lowest deviation from all experiments on average.

4.3.3 | Results

Figure 7 shows the resulting $\bar{E}_i^{\mathrm{s}}$ in comparison with the experimentally obtained values. For all computations, the mean value of the two experiments in each direction done for a single specimen was used for $\bar{E}_i^{\mathrm{m}}$. For Fit 1 the predicted values for $\bar{E}_2^{\mathrm{s}}$ and $\bar{E}_3^{\mathrm{s}}$ (which are only based on $\bar{E}_1^{\mathrm{s}}$) are clearly underestimated. The relative differences to the mean value of the experiments are 27.8% and 20.1% for $i = 2$ and $i = 3$, respectively. Nevertheless, the anisotropy is predicted correctly in a qualitative sense and in fact was discovered first in the simulation before conducting experiments in different directions. While interesting in this regard, the additional experiments may also serve as a basis for the parameter identification in Fit 2 as explained above. Here the errors (now non-zero for all directions) are more distributed and determined as 13.7% ($i = 1$), 6.5% ($i = 2$), and 4.5% ($i = 3$). Summarizing, the results show that a major part of the anisotropy can be attributed to the geometry. Whether this is truly the only origin for the anisotropy cannot be answered from the limited data that is available. However, it is expected that the assumption of an isotropic bulk material serves well as a basis for upcoming characterizations of the foam's dynamic properties and investigation of its acoustic behavior.

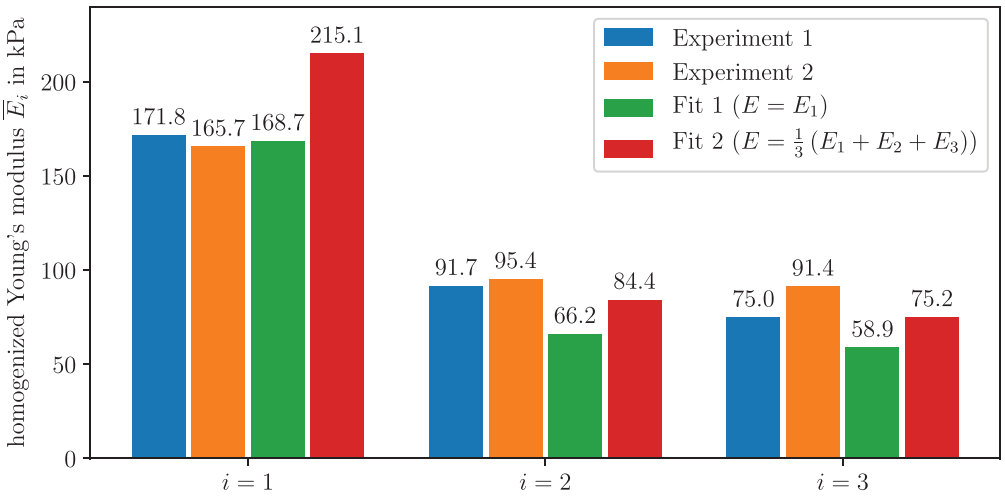

FIGURE 7 Homogenized Young's modulus obtained from experiments and simulations considering each coordinate axis.

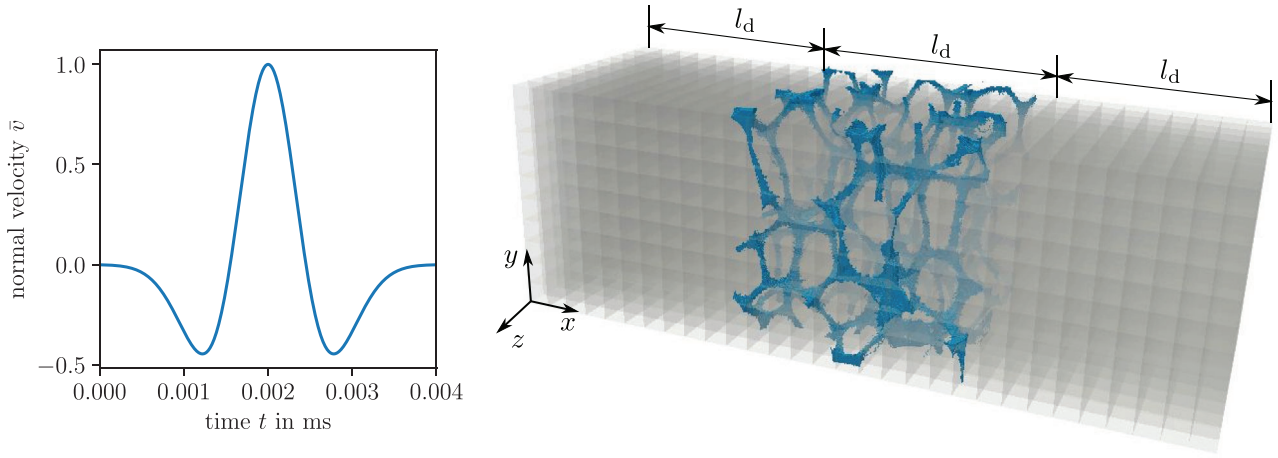

FIGURE 8 Applied velocity signal (left) and simulation domain (right) of the dynamic analysis.

5 | FULLY RESOLVED DYNAMIC ANALYSIS

In this section, we present an exemplary dynamic analysis of a foam sample using the vibroacoustic coupling approach outlined in Section 2. Figure 8 (right) illustrates the problem domain. As before, a foam specimen with edge length l_d is considered. It is immersed into a fluid domain which is extended in the x-direction on both sides. A velocity signal (see Figure 8 [left]) is applied as a plane wave by a time-varying Neumann boundary condition on the boundary in the y-z-plane. The signal corresponds to a Ricker wavelet with a central frequency of $f = 100$ kHz. We have previously used the same signal in ref. [17] and refer to it for further details. Homogeneous Neumann boundary conditions are assumed on all outer boundaries. The changes monitored in the signal as it passes through the foam are determined by observing it on both sides of the foam. In later studies, similar simulation setups will be used to characterize the foam material in terms of (bulk and homogenized) viscoelastic material models. Here, we only consider a specimen of size $l_d = 1.6$ mm, which is not expected be sufficient for a characterization. Instead, we use this exemplary problem to study the influence of the α-stabilization.

5.1 | Simulation setup

The structure domain is discretized using $n^e = 20$ elements in each direction which yields an element size of $h = 0.08$ mm. The polynomial order is set to $p = 3$ and the octree depth is set to $k = 6$. The fluid mesh is discretized using elements of

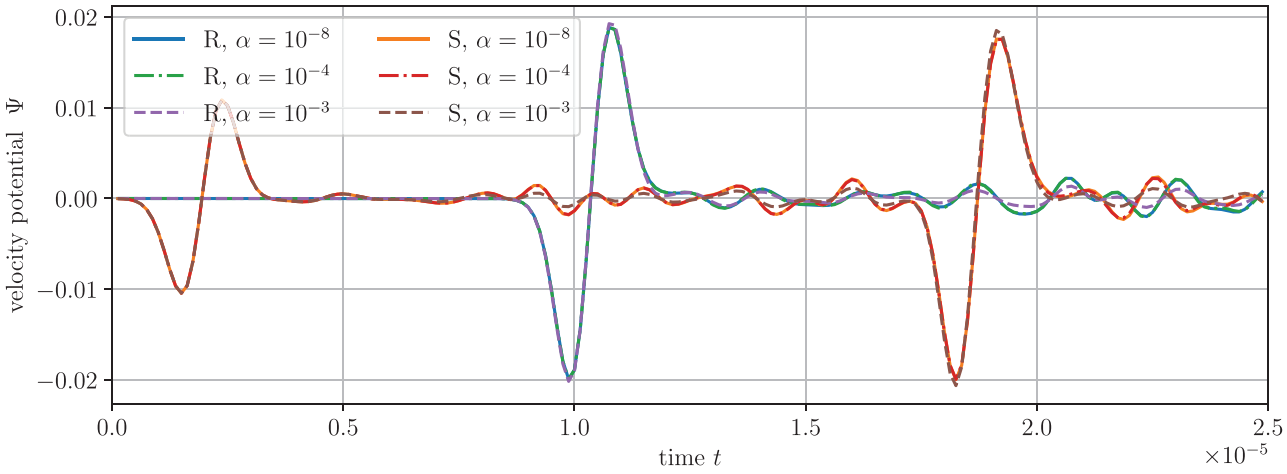

FIGURE 9 Results of the dynamic analysis: signal at sender (S) and receiver (R) side for varying $\alpha^{\min}$.

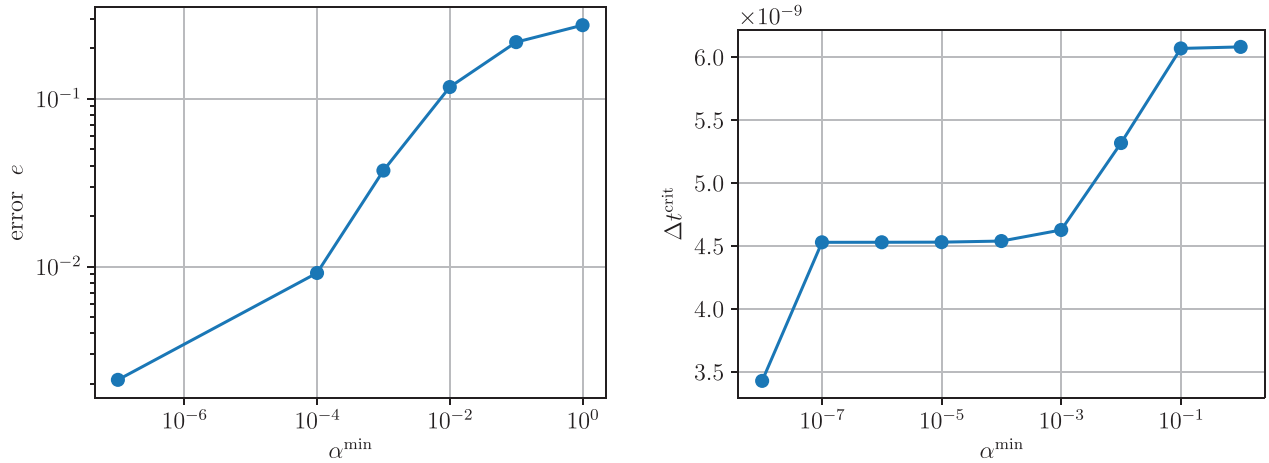

FIGURE 10 Results of the dynamic analysis: approximation error (left) and critical time step size (right) for varying $\alpha^{\min}$.

the same type and size. The interface quadrature cells are generated using 32 subdivisions. The axis-aligned edges of the triangles have the same length as the edges of cells on the lowest level of an octree with depth $k = 5$. According to the previous study it is not expected to obtain highly accurate results using this discretization. However, it admits an investigation of the α-stabilization on the accuracy and the critical time step size and showcases the simulation pipeline in a transient setting.

A time interval of 0.025 ms is considered in the simulation and a time step size of $\Delta t = 10^{-9}$ is used. This makes it possible to simulate the problem even with moderate values for $\alpha^{\min}$ and to compare the results for different choices of $\alpha^{\min}$.

5.2 | Results

Figure 9 shows the velocity potential recorded at two points S (on the sender side at $x = 0$) and R (on the receiver side at $x = 3\,l_{\text{d}}$). For both points, $y = \frac{l_{\text{d}}}{2}$ and $z = -\frac{l_{\text{d}}}{2}$. The information contained in both, the reflected signal at S as well as the transmitted signal at R, will be used in later studies for a characterization of the foam. Already, the results for different values of $\alpha^{\min}$ show that up to $\alpha^{\min} = 10^{-4}$ no difference compared to the results obtained for the smallest value of $\alpha^{\min} = 10^{-8}$ is observed visually. However, larger values lead to noticeable differences. Figure 10 (left) shows the

relationship between $\alpha^{\min}$ and the error

$$e = \sum_{i=1}^{200} \frac{\|\Psi(R,t_i) - \Psi^{\text{ref}}(R,t_i)\|}{\|\Psi^{\text{ref}}(R,t_i)\|} + \frac{\|\Psi(S,t_i) - \Psi^{\text{ref}}(S,t_i)\|}{\|\Psi^{\text{ref}}(S,t_i)\|}, \tag{15}$$

where $t_i = i\,\frac{T}{200}$ and $\Psi^{\text{ref}}(R,t_i)$ denotes the reference solution computed with $\alpha^{\min} = 10^{-8}$. Accordingly, $\alpha^{\min} \leq 10^{-4}$ is needed to maintain an acceptable accuracy for the present study. At the same time, the critical time step size is still comparably small, see Figure 10 (right) (keeping in mind, that Δ^{crit} acc. to Equation 11 only represents an upper bound to the critical time step size of the coupled system). It is therefore of great interest to apply the mentioned eigenvalue stabilization technique from ref. [14]. We investigate its performance in the context of three-dimensional FCM simulation based on CT scans in an ongoing study.

6 | CONCLUSION

We established a fully automatic simulation pipeline based around the FCM for the analysis of foamed damping materials in the time domain. Typically, immersed boundary methods like the FCM suffer from very small critical time step sizes which arise due to the presence of cut cells with small support in the physical domain. An efficient solution using explicit time integration is therefore only possible if stabilization methods are applied. In this work, the classical α-stabilization was used, but the investigations show that the novel eigenvalue stabilization method is of great interest. Using a combination of both methods it is expected that the critical time step size can be significantly increased without a severe loss of accuracy.

While a typical application scenario for the simulation pipeline is the dynamic characterization of damping materials, we focused on the static characterization here. Using linear elastic simulation of the fully resolved foam model obtained from CT scans and comparing the results to experiments isotropic bulk material parameters could be determined that reproduce the experimentally observed anisotropic behavior on the macro scale.

In future works, the static material parameter identification process will be refined and shear tests will be considered in combination with the uniaxial compression tests done so far. Further, we plan to include viscoelastic effects into our material model using Caughey damping. The parameter identification tests will then be based on additional dynamic experiments using a shaker and an impedance tube.

ACKNOWLEDGMENTS

The authors gratefully acknowledge the support of the DFG (Deutsche Forschungsgemeinschaft) under DU 405/20-1 (grant number 503865803) and EI 1188/3-1 (grant number 497531141).

Open access funding enabled and organized by Projekt DEAL.

ORCID

Lars Radtke https://orcid.org/0000-0001-7015-8928
Paul Marter https://orcid.org/0000-0001-5937-6158
Daniel Juhre https://orcid.org/0000-0001-8997-3818

REFERENCES

1. Duvigneau, F., Luft, T., Hots, J., Verhey, J. L., Rottengruber, H., & Gabbert, U. (2016). Thermo-acoustic performance of full engine encapsulations – a numerical, experimental and psychoacoustic study. *Applied Acoustics*, *102*, 79–87.
2. Parvizian, J., Düster, A., & Rank, E. (2007). Finite cell method. *Computational Mechanics*, *41*(1), 121–133.
3. Szabó, B. A., & Babuška, I. (1991). *Finite element analysis*. John Wiley & Sons.
4. Ainsworth, M. (2004). Dispersive and dissipative behaviour of high order discontinuous Galerkin finite element methods. *Journal of Computational Physics*, *198*(1), 106–130.
5. Radtke, L., Müller, D., & Düster, A. (2021). Optimally blended spectral elements in structural dynamics: Selective integration and mesh distortion. *International Journal of Computational Methods*, *18*(10), 2150042.
6. Duczek, S., Joulaian, M., Düster, A., & Gabbert, U. (2014). Numerical analysis of Lamb waves using the finite and spectral cell methods. *International Journal for Numerical Methods in Engineering*, *99*(1), 26–53.

7. Joulaian, M., Hubrich, S., & Düster, A. (2016). Numerical integration of discontinuities on arbitrary domains based on moment fitting. *Computational Mechanics*, *57*(6), 979–999.
8. Elhaddad, M., Zander, N., Kollmannsberger, S., Shadavakhsh, A., Nübel, V., & Rank, E. (2015). Finite cell method: High-order structural dynamics for complex geometries. *International Journal of Structural Stability and Dynamics*, *15*(7), 1540018.
9. Bürchner, T., Kopp, P., Kollmannsberger, S., & Rank, E. (2023). Immersed boundary parametrizations for full waveform inversion. *Computer Methods in Applied Mechanics and Engineering*, *406*, 115893.
10. Radtke, L., Torre, M., Hughes, T. J. R., Düster, A., Sangalli, G., & Reali, A. (2024). An analysis of high order FEM and IGA for explicit dynamics: Mass lumping and immersed boundaries. *International Journal for Numerical Methods in Engineering*. Accepted for publication.
11. Leidinger, L. (2020). *Explicit isogeometric B-Rep analysis for nonlinear dynamic crash simulations* [Doctoral thesis]. Technische Universität München.
12. Faßbender, C., Bürchner, T., Kopp, P., Rank, E., & Kollmannsberger, S. (2024). Implicit-explicit time integration for the immersed wave equation. *Computers & Mathematics with Applications*, *163*, 1–13.
13. Garhuom, W., Usman, K., & Düster, A. (2022). An eigenvalue stabilization technique to increase the robustness of the finite cell method for finite strain problems. *Computational Mechanics*, *69*(5), 1225–1240.
14. Eisenträger, S., Radtke, L., Garhuom, W., Löhnert, S., Düster, A., Juhre, D., & Schillinger, D. (2024). An eigenvalue stabilization technique for immersed boundary finite element methods in explicit dynamics. *Computers & Mathematics with Applications*, *166*, 129–168.
15. Dauge, M., Düster, A., & Rank, E. (2015). Theoretical and numerical investigation of the finite cell method. *Journal of Scientific Computing*, *65*(3), 1039–1064.
16. Marter, P., Radtke, L., Eisenträger, S., Düster, A., & Juhre, D. (2024). Experimental characterization of acoustic damping materials. *Proceedings in Applied Mathematics and Mechanics*. Submitted for publication.
17. Radtke, L., Marter, P., Duvigneau, F., Eisenträger, S., Juhre, D., & Düster, A. (2024). Vibroacoustic simulations of acoustic damping materials using a fictitious domain approach. *Journal of Sound and Vibration*, *568*, 118058.
18. Bathe, K. J. (1996). *Finite Element Procedures*. Prentice Hall.
19. Zienkiewicz, O. C., & Taylor, R. L. (2000). *The finite element method – solid mechanics* (5th ed., Vol. 6). Butterworth-Heinemann.
20. Hughes, T. J. R. (2012). The finite element method: Linear static and dynamic finite element analysis. *Dover civil and mechanical engineering*. Dover Publications.
21. Joulaian, M., Duczek, S., Gabbert, U., & Düster, A. (2014). Finite and spectral cell method for wave propagation in heterogeneous materials. *Computational Mechanics*, *54*(3), 661–675.
22. Kudela, L., Zander, N., Bog, T., Kollmannsberger, S., & Rank, E. (2015). Efficient and accurate numerical quadrature for immersed boundary methods. *Advanced Modeling and Simulation in Engineering Sciences*, *2-10*, 1–22.
23. Kudela, L., Zander, N., Kollmannsberger, S., & Rank, E. (2016). Smart octrees: Accurately integrating discontinuous functions in 3D. *Computer Methods in Applied Mechanics and Engineering*, *306*, 406–426.
24. Pető, M., Duvigneau, F., & Eisenträger, S. (2020). Enhanced numerical integration scheme based on image compression techniques: Application to fictitious domain methods. *Advanced Modeling and Simulation in Engineering Sciences*, *7*(1), 1–42.
25. Pető, M., Garhuom, W., Duvigneau, F., Eisenträger, S., Düster, A., & Juhre, D. (2022). Octree-based integration scheme with merged sub-cells for the finite cell method: Application to non-linear problems in 3D. *Computer Methods in Applied Mechanics and Engineering*, *401*, 115565.
26. Abedian, A., & Düster, A. (2017). An extension of the finite cell method using boolean operations. *Computational Mechanics*, *59*, 877–886.
27. Pető, M., Eisenträger, S., Duvigneau, F., & Juhre, D. (2023). Boolean finite cell method for multi-material problems including locally enrichment Ansatz spaces. *Computational Mechanics*, *72*, 743–764.
28. Hubrich, S., Di Stolfo, P., Kudela, L., Kollmannsberger, S., Rank, E., Schröder, A., & Düster, A. (2017). Numerical integration of discontinuous functions: Moment fitting and smart octree. *Computational Mechanics*, *60*(5), 863–881.
29. Hubrich, S., & Düster, A. (2019). Numerical integration for nonlinear problems of the finite cell method using an adaptive scheme based on moment fitting. *Computers & Mathematics with Applications*, *77*(7), 1983–1997.
30. Garhuom, W., & Düster, A. (2022). Non-negative moment fitting quadrature for cut finite elements and cells undergoing large deformations. *Computational Mechanics*, *70*(5), 1059–1081.
31. Nicoli, S., Agathos, K., & Chatzi, E. (2022). Moment fitted cut spectral elements for explicit analysis of guided wave propagation. *Computer Methods in Applied Mechanics and Engineering*, *398*, 115140.

How to cite this article: Radtke, L., Marter, P., Eisenträger, S., Juhre, D., & Düster, A. (2024). An automatic simulation pipeline for coupled simulations of acoustic damping materials. *Proceedings in Applied Mathematics and Mechanics*, *24*, e202400093. https://doi.org/10.1002/pamm.202400093